3D $LiMn_2O_4$ thin-film Electrodes for High Rate all solid-state Lithium and Li-ion microbatteries

Nouha Labyedh[a, b], Felix Mattelaer[c], Christophe Detavernier[c], Philippe M. Vereecken[a, b]

[a]imec, Kapeldreef 75, B-3001 Heverlee, Belgium
[b]M2S Department, Centre for Surface Chemistry and Catalysis, KU-Leuven (Leuven University)
[c]Department of Solid State Sciences, Ghent University, Krijgslaan 281 S1, 9000 Gent, Belgium

In this paper, we report on the fabrication of characterization of functional 3D $LiMn_2O_4$ thin-film electrodes giving a footprint capacity of 0.5 mAh/cm^2; i.e. surpassing any thin-film electrode reported thus far. Using a novel process based on a solid state reaction between electrolytic manganese dioxide (EMD) and Li_2CO_3 stacked-layers, crack-free, uniform and continuous lithium manganese oxide (LMO) thin-films were fabricated on planar and high aspect ratio microstructured substrates. The fabricated LMO films are shown to have a stoichiometry close to that of the spinel $LiMn_2O_4$ with a homogeneous element distribution through the layer. The prepared thin-films are electrochemically active reaching a volumetric capacity of 1200Ah/L; i.e. close to the $LiMn_2O_4$ spinel theoretical capacity. The few hundred nanometer thin-film morphology allows for use of both the 3V and 4V regions. The 3D LMO thin-film electrodes had 21 times the capacity of the planar LMO thin-film with similar thickness due to the area enhancement and the excellent conformal coating of the high aspect ratio micropillar substrates. An excellent rate performance was demonstrated for both the planar and on the high aspect ratio substrates where 48 % and 30 % of the theoretical $LiMn_2O_4$ capacity of is maintained at the very high C-rates of 20 C and 100 C, respectively.

Introduction:

Traditional Li-ion cells contain porous electrode layers coated with thicknesses in the order of 100 micrometer on metal current collector foils (Figure 1a). The coatings are composed of active electrode powder with a particle size varying between 2 and 20 µm, depending on the active material and intended

application.[1-3] The large amount of active material in these electrodes (typically around 50-70 vol.%) provides the high capacity to the battery. However, the full capacity of the high energy cells is only accessible for charging rates between 0.75 C and 1.5 C (or between 45 minutes to 1.5 hours of charging time) in part due to long diffusion distance for the Li-ions through the electrodes. Further, to assure good current collection, carbon additives are added to the electrode layer; the electrons are collected through the contacts with the many carbon nanoparticles which form a percolating conductive network to the current collector foil.[4-7] To increase the current or power of the battery, the porosity of the electrode can be increased to give more access for electrolyte, the volume percent of carbon can be increased to allow for more electronic contact, and the thickness of the electrodes can be decreased to shorten the diffusion distance. As such, large powder-based cells always have a trade-off between energy density and power density; i.e. both are possible but not at the same time.

Nanostructured electrode architectures have been proposed to increase the rate-performance of cells.[8-11] Indeed, the replacement of the micronsized powder by a submicron to nanosized powder electrode gives both shorter diffusion distance for the Li-ions through the active material and a large contact area between active material and electrolyte. In previous work, we indeed showed by comparison of data obtained from literature, the significant increase in rate performance for nanoparticles and nanorods compared to microparticles for the case of lithium manganese oxide (LMO) electrodes cycled under similar conditions.[12] However, the nanopowder does not solve the issue of inefficient current collection. On the contrary, to maintain the same level of contact points for the nanosized particles, more carbon additive will be required (which in its turn reduces the volumetric energy density). In the same paper, we also presented our results for sputtered LMO thin-films (25-100nm in thickness) showing the fastest rate performance. In this case, a short Li-ion diffusion path is provided together with an excellent current collection scenario (electrons and ions) as the continuous electrode film is now in direct contact with the underlying current collector below and with the electrolyte directly above (Figure 1b). Unfortunately, the

use of thin-film electrodes dramatically reduces the battery capacity due to the limited availability of active material; for example, a hundred micron thick LMO powder coating holds a capacity of about 3 mAh/cm^2 whereas a dense 2 micron thin LMO film only provides 0.13 mAh/cm^2. Nevertheless, thin-film architectures have been used successfully for the fabrication of all solid-state lithium and Li-ion thin-film batteries where a thin-film solid electrolyte such as LiPON is introduced between cathode and anode films.[13] Microbatteries can fill a niche of applications such as for wearable electronics, implantable devices and autonomous sensors in need of specialized micro-storage solutions. As the space is the limiting factor for these applications, the footprint capacity (mAh/cm^2) is a more commonly used for benchmarking. Often the cells can not be more than a few millimeters thick also. As microbatteries inherently can hold only limited capacity, the fast charging characteristics of thin-film batteries is very attractive (C-rates >10C or re-charging in few minutes). Unfortunately, thin-film batteries with planar geometry (as in Figure 1b) have too low capacity (<0.3 mAh/cm^2) for practical use beyond on-chip backup power [16]. As a solution for the low capacity of planar thin-film batteries, the concept of 3D thin-film Li-ion batteries has been introduced.[14-17] Here, the complete cathode/electrolyte/anode thin-film stack is coated over 3D microstructured current collector substrates. The increased effective surface area increases the actual amount of active material per footprint area. As the film thicknesses are kept thin (typically <500nm), the fast (dis)charging kinetics typical for the thin-film battery is maintained. Hence, the surface enhancement of the 3D thin-film all solid-state batteries combines both high rate performance and increased footprint capacity (mAh/cm^2). More details on the progress toward the 3D all solid-state thin-film Lithium and Li-ion batteries and the prognosis in capacity of such microbatteries can be found in recent publications of our group.[16-17]

Conformal deposition of thin-film electrode materials over microstructured substrates has been shown for e.g. MnO_2 and CuSb by electrochemical deposition (ECD)[18-19] and TiO_2 by chemical solution deposition (CSD) where conformal coating was demonstrated by spray coating and atomic layer

deposition.[20-21] To our knowledge, conformal $LiMn_2O_4$ thin-films deposition on high aspect ratio substrates has not been demonstrated before. In this paper, we report for the first time on the fabrication of conformal and functional LMO thin-films of several hundred nanometers thick over dense micropillar arrays with aspect ratio of 21. The LMO thin-films are fabricated by a solid state reaction upon thermal treatment between an electrolytic manganese dioxide (EMD) film and a superposed Li_2CO_3 layer. The Li_2CO_3 was deposited either by chemical solution deposition (CSD) or atomic layer deposition (ALD). We have demonstrated the fabrication of continuous and crack-free LMO thin-films. These thin-films have a stoichiometry close to that of $LiMn_2O_4$ with homogeneous elements distribution through the layer. It was also shown that the fabricated thin-films contain a fraction of an electrochemically MnO_2 next to the spinel $LiMn_2O_4$. The LMO thin-films reach about the full capacity of $LiMn_2O_4$ at low C-rate of 0.1 C. The fabricated LMO thin-films showed an excellent rate performance where 48 % and 30 % of the spinel $LiMn_2O_4$ theoretical capacity were reached at the high charging rates of 20 C and 100 C, respectively.

Results and discussion

Thin-films of $LiMn_2O_4$ were fabricated by a solid state reaction between a nanoporous MnO_2 precursor film and a superposed Li_2CO_3 layer by thermal annealing according to the following chemical reaction (Equation 1):

$$4MnO_2(s) + Li_2CO_3(s) \rightarrow 2LiMn_2O_4(s) + CO_2(g) + 1/2O_2(g) \quad (1)$$

First, $LiMn_2O_4$ thin-films were fabricated and characterized on planar substrates. Next, the fabrication of conformal $LiMn_2O_4$ thin-films was demonstrated on the high aspect ratio pillar arrays using the optimum process conditions obtained from the planar study. A nickel metal current collector was used for the planar and the 3D substrates.

A. $LiMn_2O_4$ thin-films on planar substrates:

Nanoporous MnO_2 thin-films were galvanostatically deposited on Ni coated silicon substrates foreseen with a TiN diffusion barrier. The anodic electrodeposition of MnO_2 is generally known as "electrolytic manganese dioxide" or EMD in short. The EMD films were deposited at a current density of 2.5 mA/cm^2 for 1 s (nucleation step) and then at 0.5 mA/cm^2 for 200 s (film growth step). This resulted in a 350 nm thick EMD film as confirmed from SEM cross sectional imaging (Figure S1). A film porosity of ~70 % was inferred from the Mn content obtained from RBS measurements which would correspond to an equivalent thickness of 115 nm in case of a dense MnO_2 film (density of MnO_2 = 5.03 g/cm^3). After deposition, the films were rinsed with water and dried in an oven at 350 °C for 120 min in air. More details on the electrochemical deposition and the properties of the obtained thin EMD layers can be found elsewhere.[22] Next, a Li_2CO_3 layer was deposited on top of the EMD thin-film by either chemical solution deposition (CSD) or by atomic layer deposition (ALD). For the CSD process, a citrate based Li-precursor solution was spin coated and thermally treated to form Li_2CO_3 (see experimental section). The stoichiometry of the deposited film was confirmed to be that of Li_2CO_3 by Elastic Recoil detection analysis (ERDA) (see table S1). An equivalent Li_2CO_3 film thickness of 158 nm was determined from the Li content and considering a Li_2CO_3 dense film (density of crystalline Li_2CO_3 = 2.11 g cm^{-3}). Note that the given thickness is that for Li_2CO_3 deposited on a TiN substrate and might be slightly different in the case of Li_2CO_3 coating on EMD films. For the ALD Li_2CO_3 a ~400 nm thick film (SEM thickness) was deposited on top of the EMD thin-film as shown in Figure 2(a) and (a'). In both cases, the amount of Li_2CO_3 provided exceeds what is needed to convert the MnO_2 to $LiMn_2O_4$. Indeed, from Eqn. 1 it follows that only 58 nm Li_2CO_3 are needed to convert the 115 nm MnO_2. The Li_2CO_3 excess was removed after the SSR by rinsing the sample with water (see experimental section). To investigate the phase formation during the solid state reaction of Eqn. 1, in-situ XRD measurements were done on the Ni/EMD/Li_2CO_3 thin-film stacks upon thermal annealing in ambient atmosphere (Figure 3(a)). The in-situ XRD experiments were performed at a temperature ramp rate of 0.2 °C/s while capturing XRD patterns between 15° to 35° 2Θ angle range which

captures the (120) γ-MnO_2 peak, the (111) and (220) LMO peaks, the (101) anatase TiO_2 peak and the (110) rutile TiO_2 peaks. At low temperatures, only the γ-MnO_2 peak can be seen which sharpens with increasing the temperature. From a temperature of 300°C on, the $LiMn_2O_4$ peak appears indicating the start of the formation of a crystalline $LiMn_2O_4$ material at this temperature. The γ-MnO_2 peak persists till 400 °C before it completely disappears indicating that the solid state reaction takes at least 500 seconds (8.3 min) under these conditions. At high temperature, Mn_2O_3 is formed, as can be seen from the two faint peaks appearing above 30°. At this temperature, Mn_2O_3 is more stable than MnO_2. As an excess of Li_2CO_3 was used, and the γ-MnO_2 peak disappears completely, it is unlikely that this is related to a remaining fraction of MnO_2 that reduces thermodynamically. Rather, this could indicate losses of lithium from the $LiMn_2O_4$, limiting the $LiMn_2O_4$ to about 600°C in air. It is also important to mention that in the 15°-35° 2Θ range other MnO_2 phases diffraction peaks could be detected as well. These peaks are: the (120) γ-MnO_2 peak; the (110) β-MnO_2 peak; the (002) δ-MnO_2 peak and the (200) and (310) α-MnO_2 peaks. For our Ni/EMD/Li_2CO_3 sample only the (120) γ-MnO_2 peak is detected. This indicates that the annealed EMD (at 350 °C for 120 min in air) films are only composed of the γ-MnO_2 phase.

At diffraction angles 25.4° and 27.4°, two additional peaks are observed in Figure 3(a), related to TiO_2 (anatase and rutile). These features start forming at 540°C and are due to the oxidation of the TiN layer underneath the Ni current collector. This would imply that also the sandwiched Ni layer is oxidized at this point. Therefore, as a reference, the Ni coated substrate was measured by in-situ XRD under the same annealing conditions (Figure 3(b)). here, the 2Θ range was set between 32.5^o and 52.5^o to monitor: the (111) and (200) Ni peaks; the (111) and (200) NiO peaks; the (111) and (200) TiN peaks; the (101), (200), (111) and (210) rutile TiO_2 peaks; and the (103), (004), (112) and (200) anatase peaks. The oxidation of Ni to NiO starts already at around 410 °C, as indicated from a shift in the Ni peaks to lower 2Θ angles, indicating lattice stretching, for example from 44.8° at room temperature to 44.2° at 635°C, at which temperature the Ni peak is consumed completely. Secondly, the appearance of NiO peaks at 37.0° and

43.2° starts at 445°C, indicating this as a high-temperature threshold for the Ni in the current collector. Here also, the TiN oxidation is observed by the appearance of rutile TiO_2 at 650°C. Hence, from the in-situ XRD measurements we can conclude that the temperature window for the solid state reaction on Ni current collector should be between 300 °C and 410 °C.

To confirm these conditions, a film was ramped at the same 0.2°/s ramp rate to 350°C, and held at that temperature isothermally for 1 hour. Figure 4 shows the phase formation for the Ni/EMD/Li_2CO_3 stack under these conditions. The $LiMn_2O_4$ peaks appears again during the temperature ramp at 300°C. The LMO peak intensity rises to the isothermal section of the anneal and rises further during the first minute of the isothermal, but then remains constant during the remainder of the isothermal. This indicates that the LMO conversion happens very fast. It is therefore suspected that the conversion reaction in Figure 3(a) has already started before the actual formation of the crystalline $LiMn_2O_4$ spinel phase. Indeed, the γ-MnO_2 diffraction peak intensity starts to decrease from the start of the measurement; i.e. well before the onset of the LMO spinel peak. Also, the MnO_2 diffraction peak is sharpening with annealing time. Hence, it is believed that γ-MnO_2 is first partially lithiated through solid state redox reaction with Li_2CO_3 according to:

$$2Li_2CO_3(s) + 4MnO_2(s) \rightarrow 4LiMnO_2(s) + 2CO_2(g) + O_2(g) \quad (2)$$

At a certain critical concentration of $LiMnO_2$ in the γ-MnO_2, recrystallization to spinel $LiMn_2O_4$ occurs. Further details on the reaction mechanism will be the subject of a follow-up paper. Interestingly, during the long isothermal, no NiO or TiO_2 features are observed, indicating that these conditions are good for a full LMO conversion without any current collector oxidation.

It was decided, based on the above in-situ XRD results, to perform the MnO_2 conversion to $LiMn_2O_4$ by annealing the Ni/EMD/Li_2CO_3 stack at 350 °C for 120 min in air. After annealing, the sample is immersed in water for 5 min to remove the Li_2CO_3 excess and then dried at 350 °C for 120 min in air. Figure 5 (a) shows the XRD pattern of the Ni/EMD/Li_2CO_3 stack after annealing, rinsing and drying. The characteristic

spinel $LiMn_2O_4$ diffraction peaks are observed together with the Ni and TiN current collector diffraction peaks. No clear MnO_2 diffraction peak was detected in this case. Note that here the sample was annealed at 350 °C for 120 min in air twice, the first one directly after the Li_2CO_3 deposition and the second after the SSR and the rinsing of the Li_2CO_3 leftover.

Figure 2 (b) and (b') show the SEM images of the Ni/EMD/Li_2CO_3(ALD) sample after annealing, rinsing and drying. A 420 nm thick continuous film can be observed on top of the Ni current collector layer. From Mn content obtained by RBS analysis an equivalent thickness of 140 nm dense $LiMn_2O_4$ film is estimated assuming that all the MnO_2 was converted (density of $LiMn_2O_4$ = 4.28 g/cm^3). Hence, in this case, the fabricated LMO film has a porosity of 66 %; i.e. close to the 70% for MnO_2.

In addition, the ERDA results of converted stack show that the film has a stoichiometry of Li=12.4 at.%; Mn=31.2 at.%; O=52.1 at.%; C=0.7 at.% and H=3.6 %. The hydrogen indicates the presence of crystal water remaining after conversion and drying. After correction for 1.8 % water, a stoichiometry of Li=13.1 at.%; Mn=33.0 at.%; O=53.2 at.% and C=0.7 at.% is obtained; i.e. close to that of $LiMn_2O_4$ spinel (Li=14 at.%; Mn=29 at.%; O=57 at.%). The higher Mn to O ratio could indicate to the presence of some Mn_2O_3 impurities, even though not apparent in the XRD. The depth profile of figure 5 (b) shows a uniform distribution of Li, Mn and O throughout the film indicating full and uniform conversion of the MnO_2 from top to bottom.

Figure 6 shows the cyclic voltammogram of the lithium manganese oxide (LMO) thin-film obtained by the solid state conversion of the Ni/EMD/Li_2CO_3 stack. In the same figure, the cyclic voltammogram of a 100 nm $LiMn_2O_4$ spinel film is shown to compare its electrochemical performance to that of our fabricated LMO by SSR. The $LiMn_2O_4$ reference film was deposited by RF-sputtering on a Pt current collector and crystallized by annealing at 800 °C for 30 min in O_2 (see experimental section). In what follows, we will use LMO for the converted film and $LiMn_2O_4$ for the sputtered spinel reference. Both cyclic voltammograms

show two sets of redox peaks centered around 4 V and 3 V vs. Li^+/Li. The redox peaks around 4 V are exclusively attributed to $LiMn_2O_4$ according to:

$$Mn_2O_4 + Li^+ + e^- \leftrightarrow LiMn_2O_4 \qquad (4.0 \text{ V and } 4.13 \text{ V vs. } Li^+/Li) \qquad (3)$$

However, the redox peaks centered around 3 V vs. Li^+/Li can either be attributed to the Li-ion intercalation reaction for spinel $LiMn_2O_4$ as follows:

$$LiMn_2O_4 + Li^+ + e^- \leftrightarrow Li_2Mn_2O_4 \qquad (2.95 \text{ V vs. } Li^+/Li) \qquad (4)$$

or to the Li-ion intercalation reaction for γ-MnO_2 where the electrode reaction is as follow:

$$MnO_2 + Li^+ + e^- \leftrightarrow LiMnO_2 \qquad (2.9 \text{ V vs. } Li^+/Li) \qquad (5)$$

Note that for both spinel $LiMn_2O_4$ and γ-MnO_2, the reaction can be complete, i.e. ($0<x<1$) with x the level of lithiation.[23-24]

As illustrated in equations 4 and 5, there is a 0.05 V potential difference between the formal potential of the Li-ion intercalation reaction for $LiMn_2O_4$ and that for MnO_2. The formal potential can be obtained from the difference in peak potential, the provided diffusion coefficients are the same for oxidation and reduction.[25] The average peak potentials of the redox peaks around 3 V were found to be 2.95 V and 2.89 V for the $LiMn_2O_4$ and LMO films, respectively (see table 1). As expected for the sputtered film, the average peak potential is exactly that of the Li^+ intercalation expected for spinel $LiMn_2O_4$. However, for the LMO film the average peak position is rather that for Li^+ intercalation for MnO_2 (eq. (5)). Since the LMO film also shows the redox peaks around 4V for spinel phase, the LMO films contains both a spinel $LiMn_2O_4$ together with an electrochemically active MnO_2 fraction. Note that the ratio of 3V to 4V peak currents is much higher for the LMO film due to the contribution of both phases to the Li^+ insertion/extraction process. These observations confirm the above isothermal in-situ XRD results that showed that not all the MnO_2 was converted to $LiMn_2O_4$ after the SSR. Interestingly, our fabrication technique is still capacity-wise profitable as the MnO_2 is now electrochemically active in contrast to the as deposited MnO_2 (EMD). In fact, in previous work it was shown that as-deposited EMD films are poorly

active for films thicker than 50nm.[22] Note that the cyclic voltammogram for the LMO films contains a significant capacitive component which is due to the porous nature of the converted film.

Table 1. Anodic/cathodic peak positions, the average peak potentials and the potential difference between the anodic and cathodic peaks from the redox peak couples around 3V of the LMO and $LiMn_2O_4$ films for cyclic voltammograms at 10mV/s in Figure 6.

Sample	Cathodic peak potential (V vs. Li^+/Li)	Anodic peak potential (V vs. Li^+/Li)	Average peak potential (V vs. Li^+/Li)	Potential difference between the anodic and cathodic peaks (V)
LMO	2.61	3.17	2.89	0.56
$LiMn_2O_4$	2.73	3.16	2.95	0.43

The Li-ion storage capacity for the different fractions in the LMO film was extracted from comparison of the charge under the cathodic peaks in the 3 V and 4 V regions. The capacity determined from the 4V region equals 2.71 $\mu Ah/cm^2$ and should in principle give the capacity of spinel $LiMn_2O_4$ fraction in the converted film which then corresponds to an equivalent thickness of 42.5 nm (considering the theoretical capacity of 0.63 Ah/cm^3). The capacity integrated under the 3 V peak is 6.20 $\mu Ah/cm^2$. By subtracting the spinel contribution (determined from the 4 V peak), the MnO_2 contribution to the Li^+ intercalation process is about 56%. However, this number should be considered with care as we found previously that for small $LiMn_2O_4$ spinel crystal sizes the 3V redox peaks can dominate the Li^+ insertion/extraction process.[12]

Figure 7 shows results for galvanostatic lithiation and delithiation of our LMO thin-films at charging rates between 0.1 C and 100 C. The current density corresponding to 1 C rate is 17.8 $\mu A/cm^2$ based on the Mn content of the films obtained from RBS (66.4 $\mu mole/cm^2$) and for complete reversible conversion of Mn(IV) to Mn(III). Figure 7 (a) shows the potential-capacity curves of the lithiation and delithiation measurements done at 1, 5 and 20 C. All potential-capacity curves display potential plateaus around 4 V and 3 V vs Li^+/Li in accordance with the peaks in the cyclic voltammogram in figure 6. Figure 7 (b) shows the lithiation capacities normalized to the $LiMn_2O_4$ equivalent thickness for different C-rates. A material capacity of 1.18 Ah/cm^3 was reached over full voltage range (4.4V-2.4V) at slowest C-rate of 0.1 C which

is close (93 %) to the theoretical capacity (1.27 Ah/cm^3) of the spinel $LiMn_2O_4$. Note that the actual volumetric capacity of the LMO films is only 34 % as the films are porous. The capacity changes only slightly from 0.1C to 1C (1.09 Ah/cm^3 for the first measurement at 1 C). For C-rates higher than 1, the capacity drops logarithmically with C-rate reaching about 0.4 mAh/cm^3 at 100 C or still an amazing ~30% of the theoretical maximum capacity. Note that the capacity values appear somewhat better from one C-rate to the next. This is the result of the capacity fading with cycling due to the well-known issue of Mn dissolution in liquid electrolytes.[26-27] For this reason exactly, the measurements were on purpose scrambled in the following sequence: 1, 5, 2, 1, 20, 10, 50, 1, 0.1 and 100. The 1C measurement was repeated three times to monitor the fading effect (figure 7 (b)): the capacity decreases from 1.09 Ah/cm^3 at the first 1C measurement to 0.75 Ah/cm^3 at the third 1 C measurement (8th measurement). The Mn dissolution issue can be addressed by implementing electrode protective coatings such as a thin solid electrolyte film as shown in [12]. Note, however, that the 3D LMO thin-film electrodes are intended for all solid-state microbatteries which will not have this cycling issue. For the sake of demonstration, we show that the Mn dissolution can be prevented by deposition a 0.5 nm thin TiO_2 protective coating by ALD on the porous LMO electrode (figure S3) [28].

Our fabricated LMO thin-film still show a competitive capacity retention where 48 % and 30 % of the spinel $LiMn_2O_4$ theoretical capacity was reached at a very high charging rates of 20 C and 100 C, respectively. This good rate performance can be attributed to the advantage of using thin-film electrode layer.[12] Importantly, please note that the capacity of our LMO thin-film reaches a capacity at 20 C equal to the maximum capacity that a bulk $LiMn_2O_4$ coating (with micron-sized particles) can reach at low C-rates. This is owing to the fact that the Li^+ insertion/extraction process for the bulk $LiMn_2O_4$ material is limited to the 4 V region due its chemical-mechanical instability in the 3 V region (Mn dissolution combined with Jahn-Teller effect). As such, bulk $LiMn_2O_4$ can only access half of the theoretical Li^+ storage capacity. Nanoscaled $LiMn_2O_4$ on the other hand, such as LMO thin-films, are stable both in the 3V and 4V region as the

mechanical strain is levitated to the surface.[12] Thus, our LMO films can access close to the maximum theoretical capacity of 1.27 Ah/cm^2 at low C-rates.

To analyze the rate performance of our films in more detail, we extracted the capacity under the 4V region (4.4-3.25 V) and 3V region (3.25-2.4 V) separately from the lithiation curves. These capacities are plotted in Figure 7 (b) and summarized in Table S 2. For all C-rates the capacity in the 3 V region was higher than in the 4 V region. This is in alignment with the cyclic voltammetry results where there also most of the film capacity was coming from the 3 V region. For example, at 1C, the total capacity of 15.53 μAh/cm^2 constituted 35 % in 4 V region and 65 % in 3V region. Furthermore, figure 7 (b) shows that the capacity in the 4 V region is constant around 0.3 Ah/cm^3 and the variation of the capacity is found in the 3V region only. Interestingly, the Li^+ intercalation in the 3V region exceeds 0.63mAh/cm^3 and thus more than the maximum capacity expected for this voltage range only.

B. Conformal $LiMn_2O_4$ thin-films on high aspect ratio micropillar arrays:

Conformal LMO thin-films were fabricated by SSR between MnO_2 and Li_2CO_3 precursors also on our Si micropillar substrate.[22,30] A nickel film was electroplated over the TiN coated Si pillars to provide additional electronic conduction and to prevent the TiN from oxidizing during the anodic MnO_2 electrochemical deposition process.[22] Figure S2 (a) shows SEM images of the Ni coated microstructured substrate with a Ni film thickness of 145 nm on the top, 195 nm on the middle and 175 nm on the bottom of the pillars. The nanoporous MnO_2 thin-film was galvanostatically deposited on the Ni coated micropillar substrates at a current density of 10.5 mA/cm^2 for 300 s (corresponding to an effective current density of about 0.5mA/cm^2 considering the 21x area enhancement for the pillars). This resulted in a MnO_2 film with a thickness of 410 nm on the top, 300 nm on the middle and 350 nm on the bottom as confirmed from SEM cross sectional imaging (figure S2 (b)). The resistive nature of the MnO_2 lead to good conformality of the EMD films.[22] The average film thickness of 350 nm is used for the MnO_2 thin-film and a porosity of 70 %, similar to the planar MnO_2 thin-film, is assumed.

Next, a Li_2CO_3 layer was deposited on top of the MnO_2 coated micropillars either by CSD or ALD; i.e. similar as for the planar case. For the CSD procedure. The Li_2CO_3 precursor solution was now drop-casted instead of spin-coated. To assure complete precursor distribution over the pillar array, the sample was placed under low vacuum for 5 min. The CSD process does not provide conformal coating but instead fills the complete space between the pillars. Due to the intrinsic layer-by-layer growth of ALD, here, conformal Li_2CO_3 films could be deposited directly over the high aspect ratio pillar arrays. To assure sufficient Li_2CO_3 precursor for complete SSR, 4500 ALD cycles were done providing a continuous and crystalline layer of Li_2CO_3 with a thickness of 430 nm on the top, 380 nm on the middle and 280 nm at the bottom of the pillars (see figure S2 (c)). Note that the ALD Li_2CO_3 process is not fully conformal due to a reservoir effect [29,31]. For both CSD and ALD cases, the solid state reaction was performed at 350 °C for 2h in air. After the reaction, the Li_2CO_3 excess was dissolved in water. Then, the sample was dried at 350 °C for 2h in air. Figure 8 shows SEM images of the LMO coated sample after the SSR reaction. In this case the ALD Li_2CO_3 precursor was used.

The 3D LMO thin-film electrodes were evaluated by lithiation and delithiation measurements at different C-rates and compared to planar equivalents of similar thickness (375 $\mu A/cm^2$ for 3D electrode at 1 C as compared to ~18 $\mu A/cm^2$ for planar electrode). Figure 9 (a) shows lithiation/delithiation curves for planar and 3D LMO films where the capacity was normalized to its maximum at 1 C. The very similar lithiation/delithiation behavior with the characteristic LMO potential plateaus centered around 3 V and 4 V vs. Li^+/Li confirms alike conversion for planar and 3D. Figure 9 (b) displays the capacity for the planar and 3D LMO thin-films electrodes for C-rate between 0.1 and 10 C. In full accordance with the area enhancement for the micropillar arrays, the capacity of the 3D LMO electrode is about 21 times larger than that of the planar electrode (specifically, 21x at 0.1 C, 20x at 1 C, 20x at 2 C, 22x at 5 C and 24x at 10 C). Remarkably, the rate performance of the 3D LMO electrode was equally good as the planar LMO, with 61 % of the theoretical capacity ($1.27 Ah/cm^3$) was reached at a high C-rate of 10 C. Hence, by making 3D

LMO thin-films we could combine the high rate performance known for thin-film electrodes together with the high capacity provided by the surface area enhancement. With a capacity of 0.47mAh/cm^2, our 3D LMO electrode has about twice the capacity of commercial planar thin-film batteries. To our knowledge, it is the highest capacity ever reported for LMO thin-film electrode, opening the door to thin-film batteries with high capacity and C-rate.

Comparison with the state-of-the-art

The thin-film fabrication technique demonstrated in this work is compatible with 3D micro-batteries. The fabrication of spinel $LiMn_2O_4$ thin-films has been already demonstrated by several deposition techniques including radio-frequency magnetron sputtering, pulsed laser deposition, atomic layer deposition (ALD), chemical vapor deposition and chemical solution deposition [12, 32-36]. However, so far, only thin-films on planar or textured surfaces (AR<5) have been shown in literature. To our knowledge, this is the first publication showing actual conformal coating of $LiMn_2O_4$ thin-films over high aspect ratio (AR > 5) features. In our case, excellent conformality was shown even for aspect ratio larger than 20; i.e. for 50 micrometers high micropillar arrays with pillar diameter and spacing of 2 micrometers. Thermal atomic layer deposition is considered as a technique which can provide excellent conformality due to the intrinsic nature of surface limited reactions. ALD of $LiMn_2O_4$ was demonstrated by the group at Oslo University in Norway [36], however, only coatings on planar stain steel substrates were shown, potentially because the ozone process could prevent conformality as shown for ALD of pure MnO_2 films using a similar ozone process [37]. In their case, 80% of the theoretical capacity was achieved at ~3 C for 80nm thin-films. As ALD processes are typically slow, they are most suited for thin-films with maximum a few tens of nanometers in thickness. When a few hundred nanometer thick coatings are needed as, for example, for the fabrication of 3D thin-film batteries on our micropillar substrates, wet chemical deposition techniques should be more suited. In this regard, chemical solution deposition (CSD) of $LiMn_2O_4$ thin-films has been explored by the group at University of Hasselt, Belgium. Films of up to ~130nm on planar substrates were

fabricated by spin coating from both aqueous and non-aqueous CSD precursor solutions [38-39]. Even though cyclic voltammograms showed electrochemical activity of (at least part of) the films, the capacity of the films nor the rate performance were reported. Interestingly, the same group has demonstrated that spray coating can be used also for conformal coating, specifically for TiO_2 and $Li_4Ti_5O_{12}$ of pillar arrays (same as those used in our work), by using diluted precursor solutions and multiple spray cycles. This method could potentially also be extended also to conformal $LiMn_2O_4$ thin-film coatings, but so far, no actual conformal coating of functional $LiMn_2O_4$ on these high aspect ratio substrates were successful [40]. The main difference of the $LiMn_2O_4$ thin-film fabrication by SSR reported in this work is that the MnO_2 layer is conformally coated first by a standard electrochemical deposition process. We have shown previously that thick and adherend films up to 1 micrometer can be electrodeposited on different current collector materials due to the resistive nature of the EMD films.[22] We have shown that the Li_2CO_3 precursor for complete SSR can either be deposited by ALD or CSD (by drop-casting or spray-coating). Thus, an advantage being that the Li_2CO_3 does not have coated with conformal thickness as long as the precursor is present all over the EMD coating. Any Li_2CO_3 excess can be removed by rinsing in water after the solid state reaction. Furthermore, the proposed technique gives more freedom to the LMO film thickness that can be deposited as we have demonstrated in this work the possibility of a conformal deposition of 350 nm MnO_2 film and in a previous work that of a 600 nm thick MnO_2 on our micropillar arrays. Conversion of the 350nm films shown in this work, gave already 0.5 mAh/cm^2 electrode capacity, i.e. double of that of planar thin-film batteries. With further optimization of cathode film thickness, a cell capacity of 1mAh/cm^2 should be feasible with current pillar arrays. With further optimization of also pillar array dimensions, 3D thin-film cell capacities of 2 to 2.5 mAh/cm^2 could be achieved as shown in a recent publication by our group [17].

Summary and Conclusions

LMO thin-films were successfully synthesized by a solid state reaction between stacked MnO_2 and Li_2CO_3 thin-films. The MnO_2 was electrochemically deposited on the current collector coated substrate and the Li_2CO_3 precursor was provided either by CSD or ALD. The XRD patterns showed the characteristic $LiMn_2O_4$ peaks and the SEM images showed a uniform morphology and a continuous film. ERD analysis showed a stoichiometry close to $LiMn_2O_4$ with a homogenous distribution of Li, Mn and O throughout the film. Nevertheless, it was shown that the LMO films still contain a fraction of an electrochemically active MnO_2 next to the spinel $LiMn_2O_4$. Our fabricated LMO thin-films approximate the full capacity of $LiMn_2O_4$ (1.27 Ah/cm^3) at low C-rates as both the 3V and 4V regions can be utilized for thin-films without capacity loss due to Jahn-Teller distortion as in the case of micron sized $LiMn_2O_4$ electrode structures. The excellent rate performance for thin-films has been confirmed on planar and demonstrated for the 3D LMO electrodes with a competitive capacity retention with 48 % and 30 % of the spinel $LiMn_2O_4$ theoretical capacity at respectively20 C and 100 C. Importantly, the capacity that our LMO thin-films reach at 20 C is equal to the maximum capacity that a bulk $LiMn_2Ok_4$ coating (with micron-sized particles) can reach at low C-rates.

LMO thin-films were also fabricated on high aspect ratio Ni coated silicon pillar arrays using our solid state conversion technique. In this case, conformal MnO_2 thin-films were electrochemically deposited and the Li_2CO_3 was provided, as on planar, either by CSD or ALD. The LMO thin-films on 3D showed similar electrochemical performance as the planar ones with excellent rate performance. In addition, 21 times higher capacity was reached with the 3D LMO thin-film than the planar ones due to the area enhancement provided by the microstructured substrate. A similar LMO thin-film fabricated by our SSR reaction technique on high aspect ratio substrates can be used as cathode layers for all solid-state 3D thin-film batteries where conformal thin-film electrolyte (LiPON for example) and electrode (TiO_2 for example) layers can be used. This will result in the fabrication of a compact all solid-state Li-ion microbatteries with higher volumetric energy density than the commonly commercialized powder based Li-ion batteries. This

high volumetric energy density is a result of the limited thickness of the electrolyte layer (~100 nm) and the absence of all types of additives (usually used in the powder based electrode layers) in the electrode layers. In addition, a high power density of such a battery is granted by the great rate performance of the thin-film electrodes.

Experimental section

Planar Ni coated substrate

150nm Ni layer was deposited on top of TiN(150nm)/Ti(15nm)/SiO_2(100nm)/Si substrate. The Ni, TiN and Ti layers were deposited by PVD (sputtering). The 100 nm SiO_2 layer is formed by thermal oxidation of a 200 mm silicon wafer.

Ni coated Si high aspect ratio micropillar arrays

Si high aspect ratio micropillar arrays were fabricated by lithography and deep reactive-ion etching on a 300 mm Si wafer. This process resulted in the fabrication of a Si micropillar arrays with 50-60 μm high, 2μm of pillar diameter and 2 μm interpillar spacing. Figure S4 shows SEM images of a TiN coated a Si micropillar array sample. After, a 23 nm TiN layer was deposited by atomic layer deposition on the Si substrate. Then, a 100 nm Ni layer was deposited by PVD (evaporation) on top of the TiN layer. This layer will be used as a buffer layer for the Ni electroplating. The Ni electroplating was done as follow: First the substrate was cleaned in an HCl (20 %) solution to remove the native acid eventually formed on the Ni buffer layer. After the sample was rinsed in water and then immediately after the sample was immerged in the deposition bath composed of 0.6 M nickel sulfate and 0.6 M boric acid. The deposition was done at 40 °C at a current density of -0.6 Ah/cm^2 for 600 s.

EMD thin-film deposition

Constant current EMD films electrodeposition was performed using a three-electrode cell where a Pt mesh counter electrode and Ag/AgCl/3M KCl reference electrode were used. The EMD deposition was performed at room temperature (21-25 °C). The deposition bath deposition is composed of an aqueous

solution of 0.5 M $MnSO_4 \cdot H_2O$ (98.0% Sigma Aldrich) and 0.5 M CH_3COONa (99.0 % Sigma Aldrich) with an addition of ~10 wt% ethanol. The EMD deposition was done at current density of 2.5 mA/cm^2 for 1s (nucleation step) then at 0.5 mA/cm^2 for 200 s (film growth step) on the planar substrates and at 0.5 mA/cm^2 for 300 s on the 3D substrates. After the EMD deposition the samples were annealed in an oven at 350 °C in air to remove the water content within the film structure.

LMO by RF-sputtering on Pt coated substrate

$LiMn_2O_4$ films were deposited by RF-sputtering on a Pt coated planar substrate. The substrate consists of silicon sample with a thermally grown 30 nm silicon oxide followed by a 10 nm TiN coating (ALD). After the substrate was annealed at 800 °C in air for 30 min to prevent an eventual outgassing during any future annealing that the sample will undergo. Hereafter, 80 nm thick Pt layer was deposited by DC sputtering. The Pt layer is used in this case as a current collector and a diffusion barrier. The $LiMn_2O_4$ thin-film was deposited by RF-sputtering on the Pt coated substrate using a 4 in. target (Neyco, France, 99.5% purity) at a power of 100 W of power and under Ar flow (25 sccm). The as-deposited amorphous $LiMn_2O_4$ film was then annealed at 800 °C for 20 min in O_2 atmosphere. A similar annealing condition is commonly used to make crystalline $LiMn_2O_4$ starting from the as-deposited amorphous one.[12]

Li_2CO_3 by chemical solution deposition

For the Li_2CO_3 spincoating and drop casting an aqueous citrate based lithium precursor was used. It is composed of lithium hydroxide (LiOH ≥ 98 %, Sigma-Aldrich), citric acid ($C_6H_8O_7$, 99 %, Sigma-Aldrich) and concentrated ammonia (NH_3, extra pure, 32 %, Merck) as starting compounds. 1.5 M LiOH precursor solutions were prepared with a pH equal to 6.7. The Li_2CO_3 was deposited by spin-coating on the planar samples and by drop casting on the high aspect ratio microstructed samples. The spincoating was done at 500 rpm for 10 s then at 3000 rpm for 30 s, followed by a short thermal treatment steps on hot plates at 110 °C for 1 min then at 280 °C for 2 min.

Li_2CO_3 by ALD

The Li_2CO_3 thin-film deposition by ALD was performed using a Picosun ALD tool (Picosun R200) and argon as a carrier gas. lithium tert-butoxide, water and carbon dioxide precursors were used. Each cycle consists of 5 s of lithium tert-butoxide pulse followed by 15 s purge at 140 °C) then 0.5s of H_2O 0.5 s followed by 15 s purge and 7.5 s of CO_2 pulse followed by 5 s purge. In total 4500 cycles were performed to make the targeted Li_2CO_3 layer with a reactor temperature of 250 °C.

Li_2CO_3 excess removal

The Li_2CO_3 excess after the SSR between the EMD and Li_2CO_3 superposed layers was removed by immersing the sample in water for 5min. Then, the sample was dried by a N_2 gun and annealed in the oven at 350 °C for 120 in air.

TiO_2 protective coating by ALD

0.5nm TiO_2 film was deposited by thermal ALD on the porous LMO planar thin film as a protective layer using TDMAT and water precursors: 4 cycles where performed with 5 s precursor pulses of 5×10^{-3} mbar alternated with pump times allowing the pressure to drop to 10^{-6} mbar. The TiO_2 thickness was measured by ellipsometry on 100 nm SiO_2 coated silicon wafers.

Annealing

The annealing experiments were performed at 350 °C for 120 min in air with a heating rate of 350 °C/min and a cooling rate of 20 °C/min using a rapid thermal annealing furnace (Heat pulse 410, AG Associates).

Material Characterization

The film morphology was investigated by Scanning Electron Microscopy (SEM) using SEM Nova 200 and Philips SEM XL30 microscopes. To prove the crystalline structure, X-ray diffraction (XRD) measurements were performed using X'Pert PRO, PANalystical system with Cu Kα radiation. A Grazing incidence mode was used in a 2θ scan range between 15 deg and 65 deg with a step size of 0.01 deg and a time per step of 0.5 s/deg. For elemental analysis, including lithium, elastic recoil detection analysis measurements were performed using a home-made ERDA system using an 8 MeV beam energy and a $Cl4^+$ ion. Rutherford

Backscattering Spectrometry (RBS) measurements were performed using a 1.523 MeV He^+ beam, a tilt angle of 11 deg and a scatter angle of 170 deg.

The ERDA was done on TiN to ovoid peak interference with the substrate. ERDA depth profile analysis was used to determine the chemical composition of the LTO films. For this type of measurements, the LTO films were grown on Si_3N_4 coated silicon substrate instead of platinum or TiN as the signals origination from the current collectors (Pt and TiN) interfere with that of LTO.

The in-situ XRD was performed in a Bruker D8 Discover using a copper X-ray source (Cu-Kα at 0.154nm). A custom-built annealing chamber was used to control the temperature and ambient. During in-situ XRD, the source was maintained at a fixed position, and a linear detector was also used stationary, resulting in a 20° 2Θ diffraction window. Integration time was chosen to obtain a resolution of 1°C in temperature, i.e. 5 seconds integration time for the 0.2°C/s ramp rates that were used in this study.

The electrochemical characterization

The electrochemical performance of the prepared LMO layers was evaluated using a three-electrode configuration with lithium metal foil as a counter and a reference electrode. The three electrodes were separated in a tefelon cell by a liquid electrolyte of 1 M of $LiClO_4$ (99.99%, Sigma-Aldrich) in propylene carbonate (anhydrous, 99.7%, Sigma-Aldrich) solvent. The setup was connected to an Auto lab PGTAT 5 potentiostat controlled by Nova 1.10 software. The electrochemical measurements were performed at room temperature in an argon filled glove-box (Pl-HE-46B-1800, Innovative Technology). Lithiation/delithiation Capacity and the rate performance were evaluated by doing cyclic voltammetry and galvanostatic lithiation and delithiation measurements. The cyclic voltammetry measurements were done in a voltage range of 2.4-4.4 V vs. Li^+/Li with a scan rate of 10 mV/s. The lithiation and delithiation measurements were done in a voltage range of 2.4-4.4V for the planar sample and 2.2-4.6 V for the 3D sample with a 60 s waiting step between the lithiation and the delithiation. 2 cycles of lithiation and

delithiation were done 2 at each C-rate and the average of the lithiation and delithiation value was taken to evaluate the film rate performance.

Acknowledgments

This work was financially supported by the 7th Framework program under the project SiNERGY (FP7-NMP-SMALL-2013-604169) and by the IWT-Flanders (Belgium) through the SBO “SoS-Lion” and “LaminaLion” projects.

References

[1] W.C. West, J. Soler, B.V. Ratnakumar, Journal of Power Sources, 2012, 204 200–204

[2] A. Sakudaa, A. Hayashi, T. Ohtomo, S. Hama, M. Tatsumisago, Journal of Power Sources, 2011, 196 6735–6741

[3] A. Sakuda, A. Hayashi, T. Ohtomo, S. Hama, M. Tatsumisago, Electrochemical and solid state Letters, 2010, 13 (6) A73-A75

[4] W. Zhang, T. Leichtwei, S. P. Culver, R. Koerver, D. Das, D. A. Weber, W. G. Zeier and J. Janek, ACS Appl. Mater. Interfaces, 2017, 9 35888−35896

[5] H. Hao, K. Chen, H. Liu, H. Wang, J. Liu, K. Yang, H. Yan, Int. J. Electrochem. Sci., 2018, 13 2329 – 2340

[6] A. Tornheim, M. He, Chi-Cheung Su, Z. Zhang, Journal of The Electrochemical Society, 2017, 164 (1) A6366-A6372

[7] M. E. Spahr, D. Goers, A. Leone, S. Stallone, E. Grivei, Journal of Power Sources, 2011, 196 3404–3413

[8] H.-W. Lee, P. Muralidharan, Riccardo Ruffo, Claudio M. Mari, Yi Cui, Do Kyung Kim, Nano Lett. 2010, 10, 3852–3856

[9] S. T. Taleghani, B. Marcos, K. Zaghib, G. Lantagne, Journal of The Electrochemical Society, 2017, 164 (11) E3179-E3189

[10] H. Xia, Z. Luo, J. Xie, Chinese Materials Research Society, 2012, 1002-0071

[11] J. Yue, F. M. Badaczewski, P. Voepel, T. Leichtwei, D. Mollenhauer, W. G. Zeier, B. M. Smarsly, ACS Appl. Mater. Interfaces, 2018, 10, 22580−22590

[12] B. Put, P. M. Vereecken, N. Labyedh, A. Sepulveda, C. Huyghebaert, I. P. Radu and A. Stesmans, ACS Appl. Mater. Interfaces, 2015, 7, 22413−22420

[13] B. Put, M.J. Mees, N. Hornsveld, A. Sepúlveda, P.M. Vereecken, W.M.M. Kessels, M. Creatore, ECS Transactions, 2017, 75 (20) 61-69

[14] P. M. Vereecken, C. Huyghebaert, ECS Transactions, 2013, 58 (10) 111-118

[15] L. Baggetto, Rogier A. H. Niessen, Fred Roozeboom, Peter H. L. Notten Adv. Funct. Mater., 2008, 18 1057–1066

[16] S. Moitzheim, B. Put, P. M. Vereecken, Advances in three-dimensional thin-film Li-ion batteries, Adv. Mater. Interfaces, 2019, 1900805

[17] S. Moitzheim, J. E. Balder, R. Ritasalo, S. Ek, P. Poodt, S. Unnikrishnan, S. De Gendt, P. M. Vereecken, ACS Appl. Energy Mater., 2019, 2, 1774−1783

[18] A. Radisic, D. J. Cott, S. Deheryan, A. S. Etman, Y. Zargouni, P. M. Vereecken, ECS Transactions, 2014, 61 (9) 1-7

[19] J. M. Mosby, Amy L. Prieto, J. AM. CHEM. SOC., 2008, 130

[20] J. van den Ham, S. Gielis, Marlies K. Van Bael, A. Hardy, ACS Energy Lett., 2016, 1, 1184−1188

[21] S. Moitzheim, J. Elisabeth Balder, P. Poodt, Sandeep Unnikrishnan, S. De Gendt, Philippe M. Vereecken, Chem. Mater., 2017, 29, 10007−10018

[22] M. Y. Timmermans, N. Labyedh, F. Mattelaer, S. P. Zankowski, S. Deheryan, C. Detavernier, Philippe M. Vereecken, Journal of The Electrochemical Society, 2017, 164 (14), D954-D963

[23] C. Liu, Zachary G. Neale, G. Cao, Materials Today V, 2016, (2) 19

[24] Eric D. Rus, Geon Dae Moon, Jianming Bai, Daniel A. Steingart, Can K. Erdonmez, Journal of The Electrochemical Society, 2016, 163 (3) A356-A363

[25] Dennis H. Evans, Kathleen M. O'Connell, Ralph A. Petersen, Michael J. Kelly, *J. Chem. Educ.*, 1983, 60 (4) 290

[26] N-S. Choi, J-G. Han, S-Y. Ha, I. Parka, Chang-Keun Back, RSC Adv., 2015, 5, 2732–2748

[2**7**] Y**.** Terada, Y**.** Nishiwaki, A**.** Nakai, F**.** Nishikawa, Journal of Power Sources, 2001, 97–98, 420-422

[28] F. Mattelaer, P. M. Vereecken, J. Dendooven, C. Detavernier, Adv. Mater. Interfaces, 2017, 4, 1601237

[29] E. Østreng, P. Vajeeston, O. Nilsen, H. Fjellvag, RSC Adv., 2012, (2) 6315

[30] N. Labyedh, B. Put, A-A. El Mel, P. M. Vereecken, Journal of The Electrochemical Society, 2018, 165 (8) B3184-B3193

[31] O. Nilsen, K. B. Klepper, Heidi Ø. Nielsen, H. Fjellvåg, ECS Transactions, 2008, 16 (4) 3-14

[32] D. Albrecht, H. Wulfmeier, H. Fritze, Energy Technol., 2016, (4) 1558–1564

[33] K. Tadanagaa, A. Yamaguchia, A. Sakudaa, A. Hayashia, M.Tatsumisagoa, A. Duranb, M. Aparacio, Materials Research Bulletin, 2014, (53) 196–19

[34] Y. H. Ikuhara, X. Gao, R. Huang, Craig A. J. Fisher, A. Kuwabara, H. Moriwake and Keiichi Kohama, J. Phys. Chem. C, 2014, (118) 19540−1954

[35] Y. Ho Rho, K. Kanamura, T. Umegaki, Journal of The Electrochemical Society, 2003, (150) A107-A111

[36] V. Miikkulainen, A. Ruud, Erik Østreng, O. Nilsen, M. Laitinen, T. Sajavaara, H. Fjellvåg, *J. Phys. Chem. C*, 2014, 118 (2) 1258–1268

[37] F. Mattelaer, P. M. Vereecken, J. Dendooven, C. Detavernier, Chem. Mater. 2015, (27) 3628−3635

[38] G. Maino, R. Carleer, W. Marchal, G. Bonneux, A. Hardy, M. K. Van Bael, DaltonTrans., 2017, (46) 14934–14946

[39] G. Maino, J. D'Haen, F. Mattelaer, C. Detavernier, A. Hardy, M. K. Van Bael, J. Mater. Chem. A, 2016, (4) 18457-18469

[40] G. Maino, 2017, Chemical solution deposition of $LiMn_2O_4$ cathodes for thin film lithium ion batteries: Following the path from precursor chemistry towards active 2D and high aspect ratio 3D layers, University of Hasselt, Hasselt, Belgium

Figures

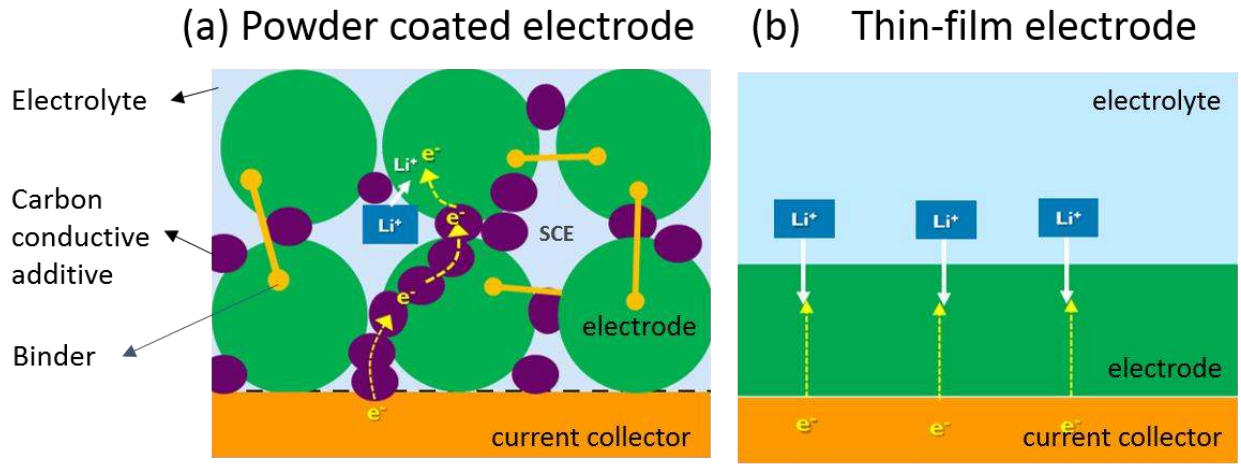

Figure 1. Schematic of 2 different electrode architectures: (a): Powder coated electrode layer were a micron-sized powder electrode material is used together with carbon additives and binders; (b): Thin-film electrode layer where a continuous film (< 1 µm) of active electrode material is directly deposited on the current collector without any additives.

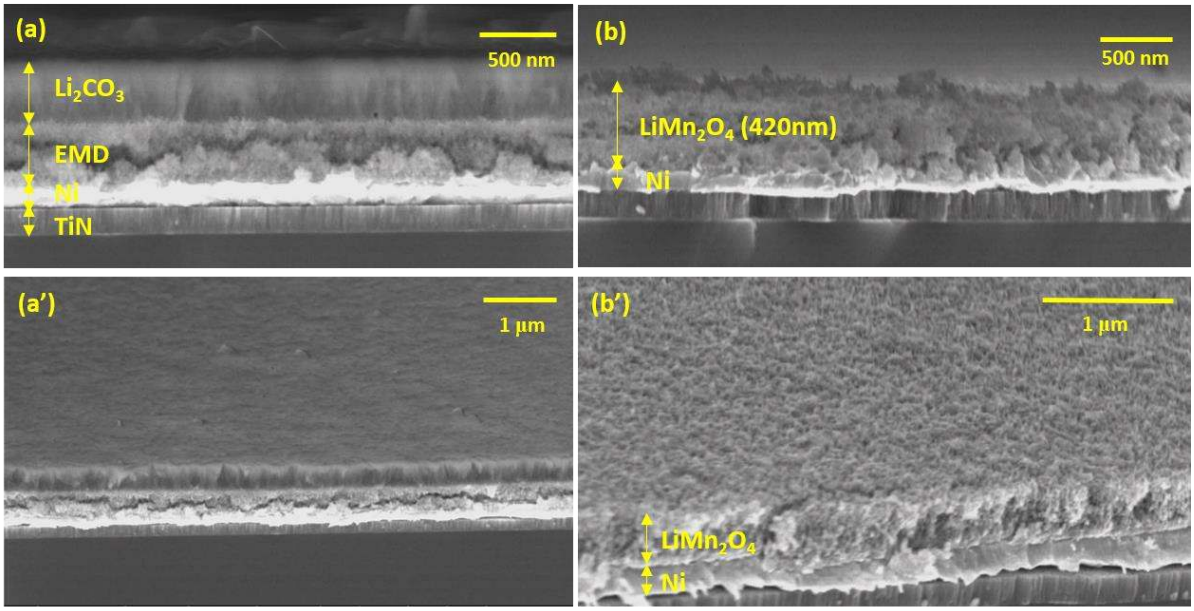

Figure 2. SEM images of: (a)&(a'): The as deposited Ni/MnO_2/Li_2CO_3 where the Li_2CO_3 layer was deposited by ALD on top of the MnO_2 layer. (b)&(b'): The Ni/LMO(420 nm) sample where the LMO was made by SSR at 350 °C, 120 min in air followed by rinsing (immersing in water for 5 min) and drying (350 °C, 120 min in air) steps.

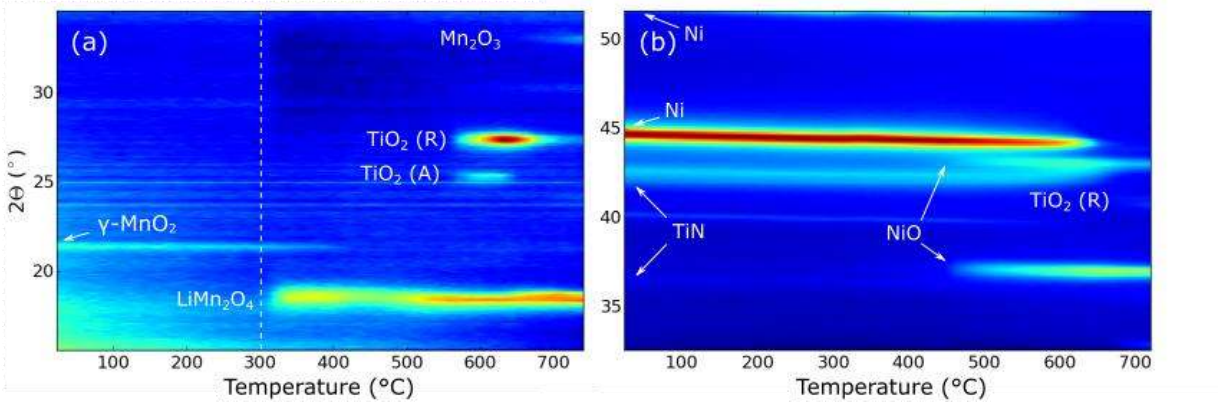

Figure 3. In-situ XRD patterns of the measurements done on: (a) Ni/MnO_2/Li_2CO_3(spincoated) sample on planar substrate; (b) Ni coated planar substrate. These measurements were done by varying the temperature from RT to 700 °C in ambient air at a ramp rate of 0.2°C/second.

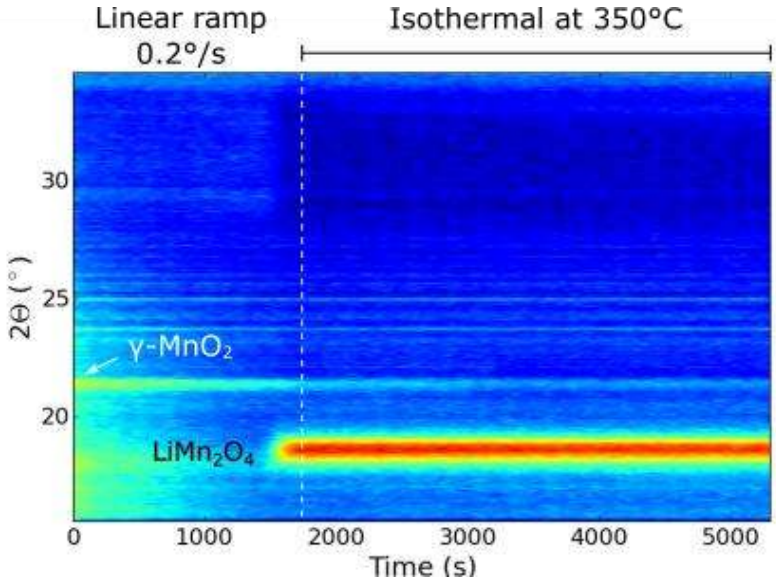

Figure 4. XRD pattern of the isothermal in-situ XRD measurement done on a Ni/MnO_2/Li_2CO_3(spincoated) on planar substrate. The temperature was ramped linearly up to 350 °C at a ramp rate of 0.2°/s, and maintained isothermally for a duration of 1 hour.

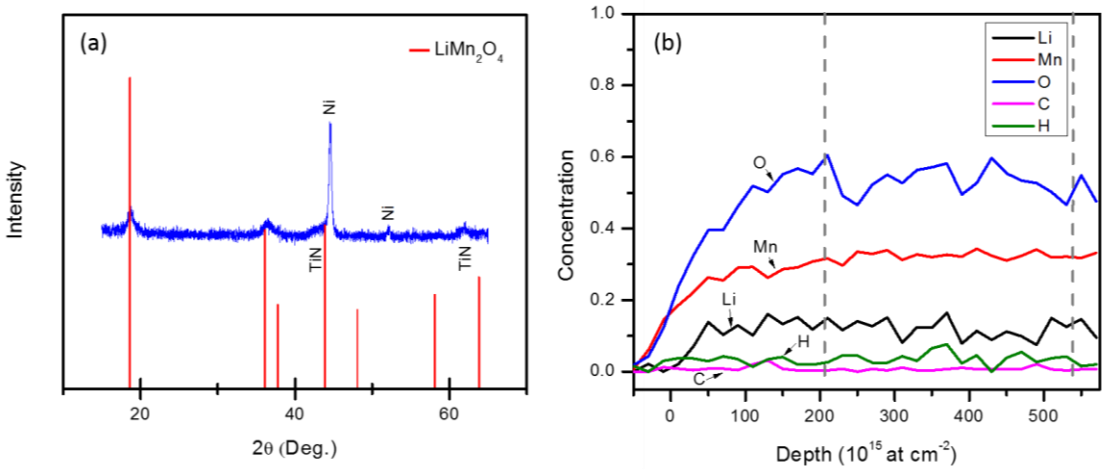

Figure 5. (a) XRD pattern of the Ni/MnO_2/Li_2CO_3 stack after annealing at (350 °C for 120 min in air), immersing in water for 5 min at RT and drying at 350 °C for 120 min in air. (b) Depth profile from the ERDA measurement performed on a Ni/MnO_2/Li_2CO_3 sample after annealing (350 °C for 120 min in air), rinsing (immersing in water for 5 min at RT) and drying (350 °C for 120 min in air). The film stoichiometry was determined from the area between the two grey dashed lines.

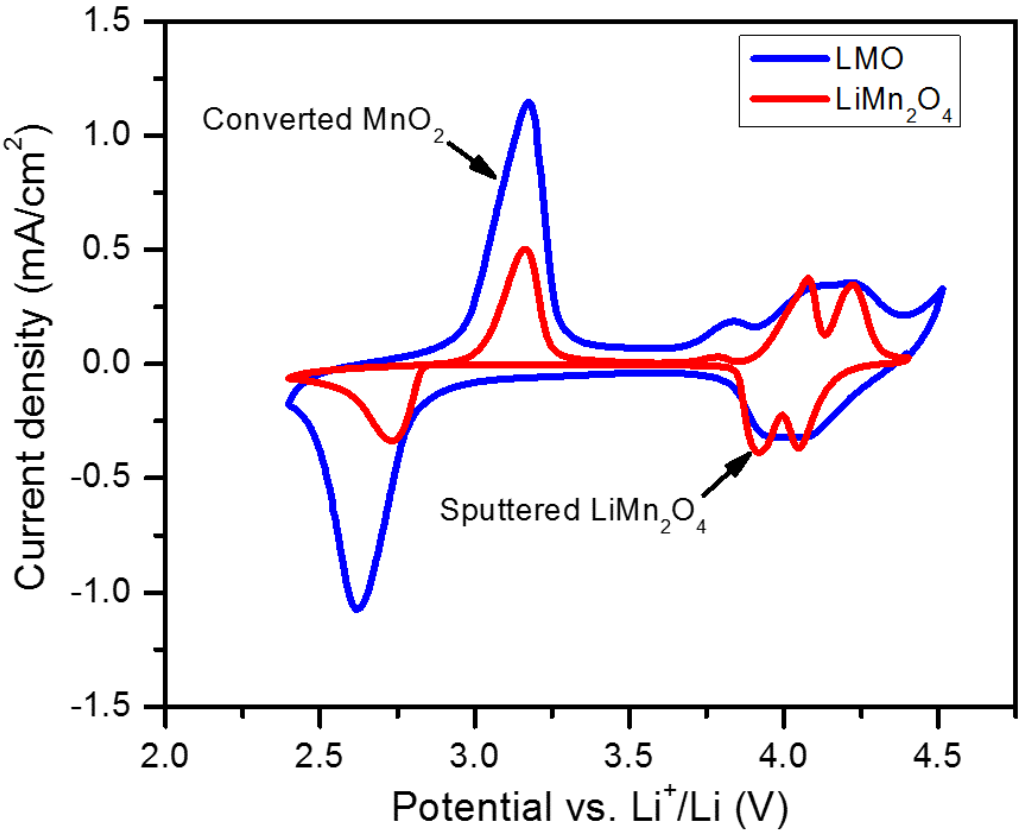

Figure 6. Cyclic voltammogram of 140* nm LMO thin-film on Ni coated planar substrate fabricated by SSR at 350 °C for 120 min in air and a 100 nm $LiMn_2O_4$ film deposited by RF-sputtering on a Pt coated planar substrate then crystallized by annealing at 800 °C for 30 min in O_2.

*equivalent thicknesses determined from RBS measurement.

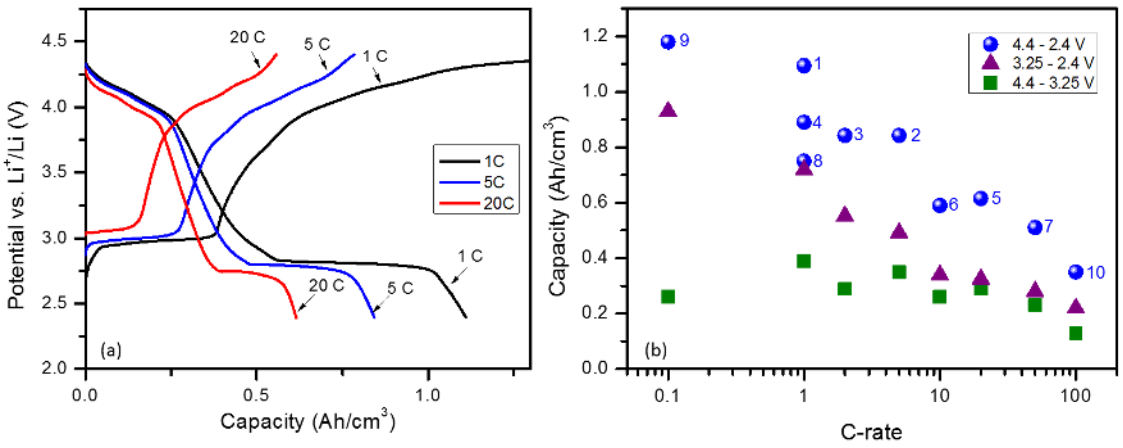

Figure 7. (a) Lithiation and delithiation curves of Ni/LMO(140 nm*) sample at different C-rates. The LMO was fabricated by a solid state reaction between MnO_2 and Li_2CO_3(spincoated) superposed layers upon thermal annealing at 350 °C for 120 min in air. After the sample was rinsed in water for 5 min then dried at 350 °C for 120 min in air. (b) Capacity reached at different C-rates from the Ni/LMO(~140nm*) sample in different potential ranges ([4.4, 2.4] = full potential range, [4.4, 3.25] = 4V region and [3.25, 2.4] = 3V region). The different C-rate measurements were done in the following sequence: 1, 5, 2, 1, 20, 10, 50, 1, 0.1 and 100.

*equivalent thicknesses determined from RBS measurement.

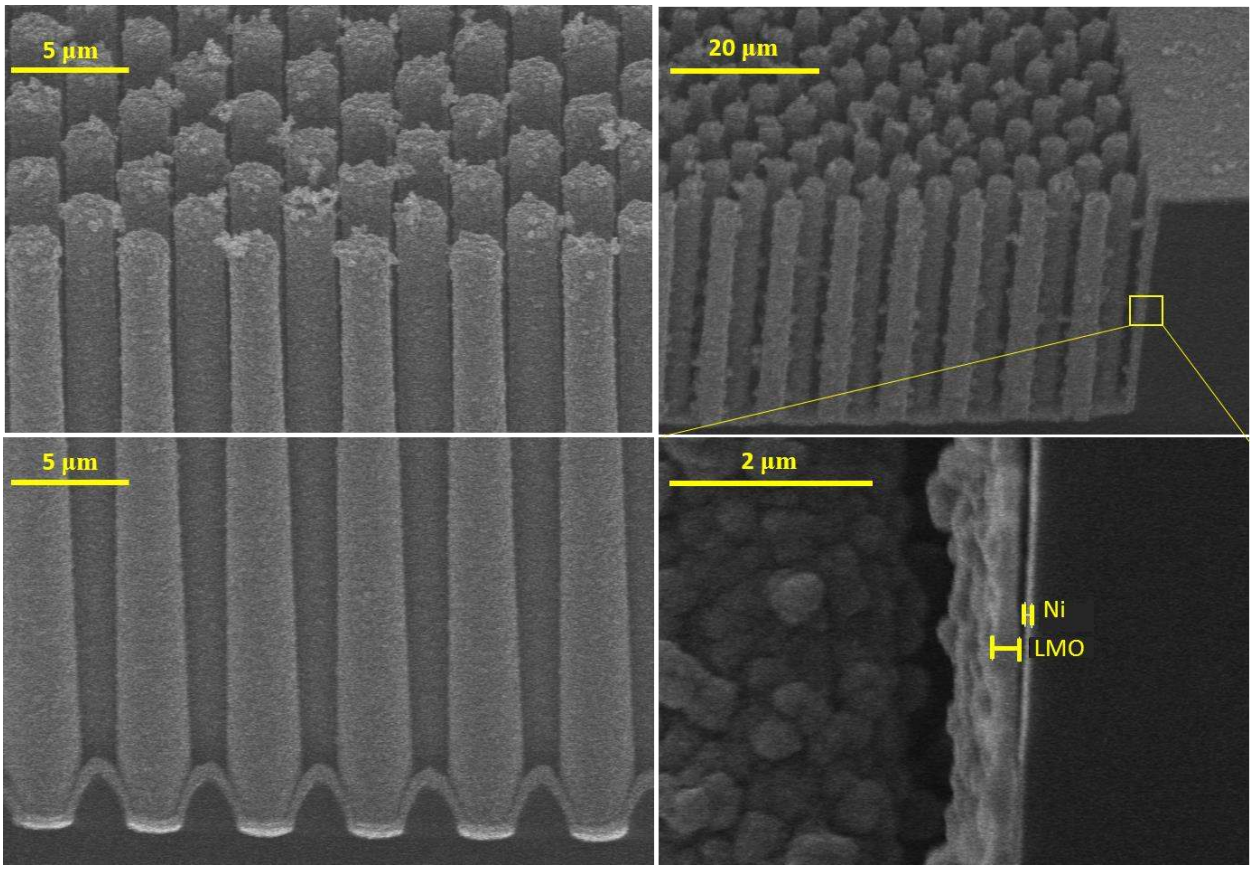

Figure 8. SEM images of Ni/LMO on the TiN coated Si microstructured substrate foreseen with a Ni buffer layer (by PVD). The LMO film was fabricated by a solid state reaction between EMD and Li_2CO_3(ALD) superposed layers upon thermal annealing at 350 °C for 120 min in air. After, the sample was rinsed in water for 5 min then dried at 350 °C for 120 min in air.

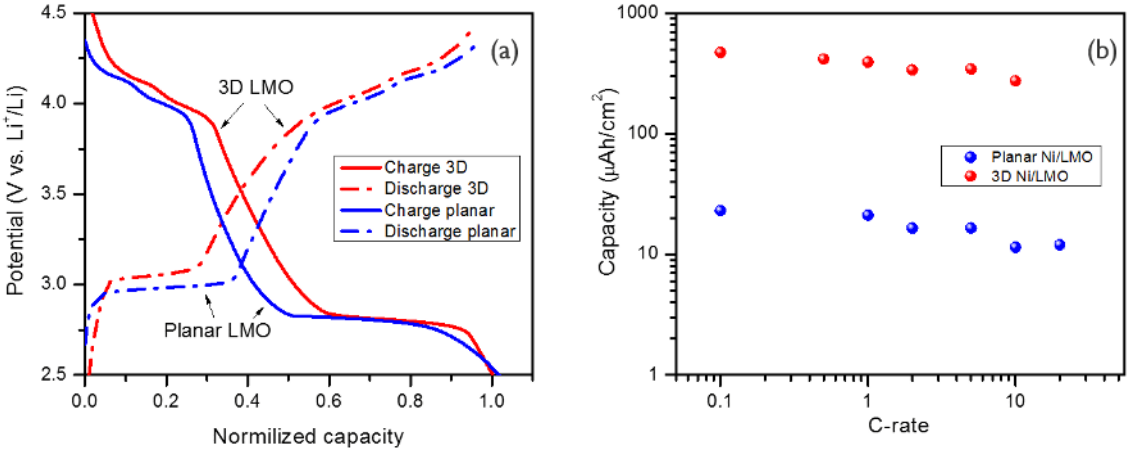

Figure 9. Results from the lithiation and delithiation measurements performed on Ni/LMO on planar and high aspect ratio micropillar (3D) substrates. (a) Lithiation and delithiation curves at 1 C where the capacity is normalized to the maximum capacity reached from each LMO film. (b) capacity reached at different C-rates from: (red dots) LMO film made by a solid state reaction on high aspect ratio micropillar (3D) substrate; (blue dots) Planar LMO film made by a solid state reaction on planar substrate.

Supplementary information

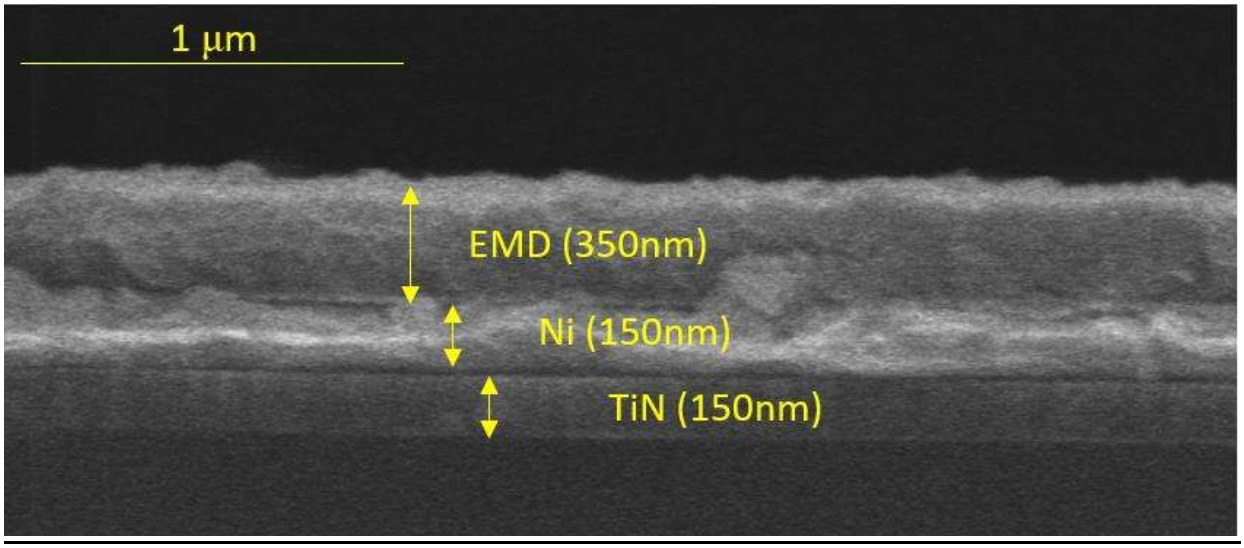

Figure S1: SEM image of a TiN/Ni/EMD sample. The EMD deposition was done at constant current density of 2.5 mA/cm^2 for 1s then 0.5 mA/cm^2 for 200 s. The sample was rinsed in water after deposition then dried at 350 °C for 120 min in air.

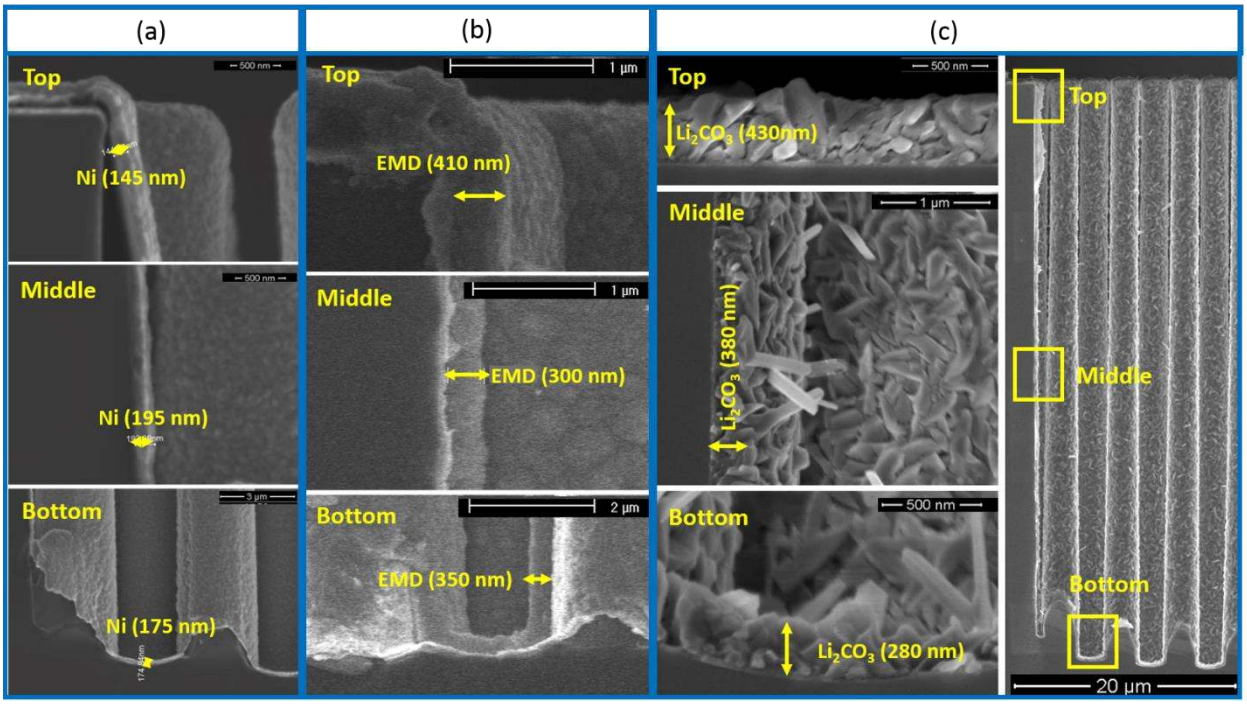

Figure S2. SEM images of: (a) TiN/Ni sample, the Ni film was electroplated on the TiN coated Si microstructured substrate foreseen with a Ni buffer layer (by PVD). (b) EMD on the Ni coated microstructured substrate; (c) Li_2CO_3 deposited by ALD on the TiN coated Si microstructured substrate.

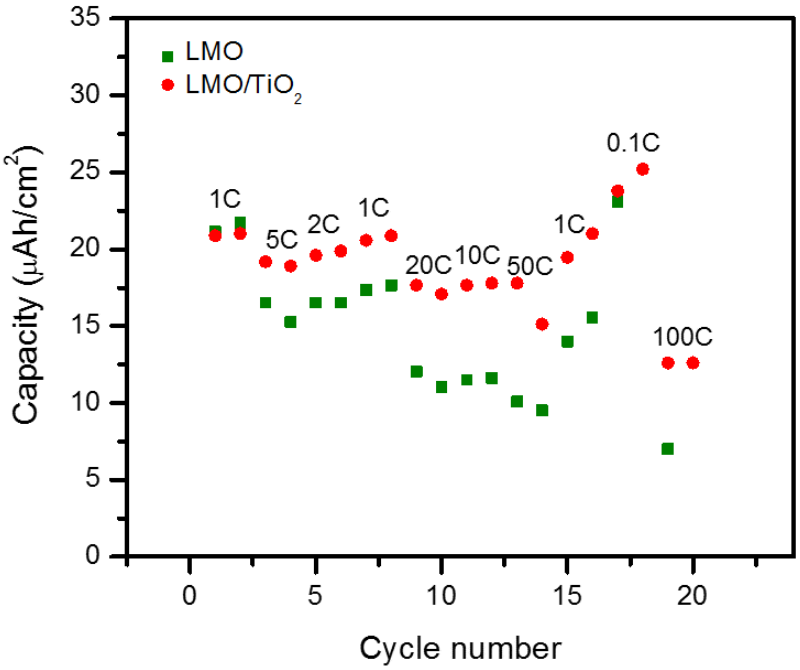

Figure S3. Lithiation capacity densities reached at different C-rates of LMO thin-films when cycled in the [2.4V - 4.4V] voltage range. Green squares: bare 420 nm (SEM thickness) LMO thin-film on Ni coated planar substrate. Red dots: 0.5nm TiO_2 coated 420 nm (SEM thickness) LMO thin-film on Ni coated planar substrate.

The rate performance of the LMO thin-film electrode with and without a 0.5nm TiO_2 protective coating is shown in figure S3. For the first cycles at 1C, both the bare and TiO_2 coated LMO thin-film give the same capacity density of 21 $\mu Ah/cm^2$. The capacity at 1C is kept around the same initial value over cycling in case of usage of TiO_2 protective coating as we excluded the Mn dissolution issue by inhibiting the direct contact between the LMO thin film and the liquid electrolyte. In addition, an improvement of the rate performance of the TiO_2 coated LMO thin film was observed, this can be due to an improvement of the interface contact. More details about the effect of protective coatings on LMO thin films can be found elsewhere.[28]

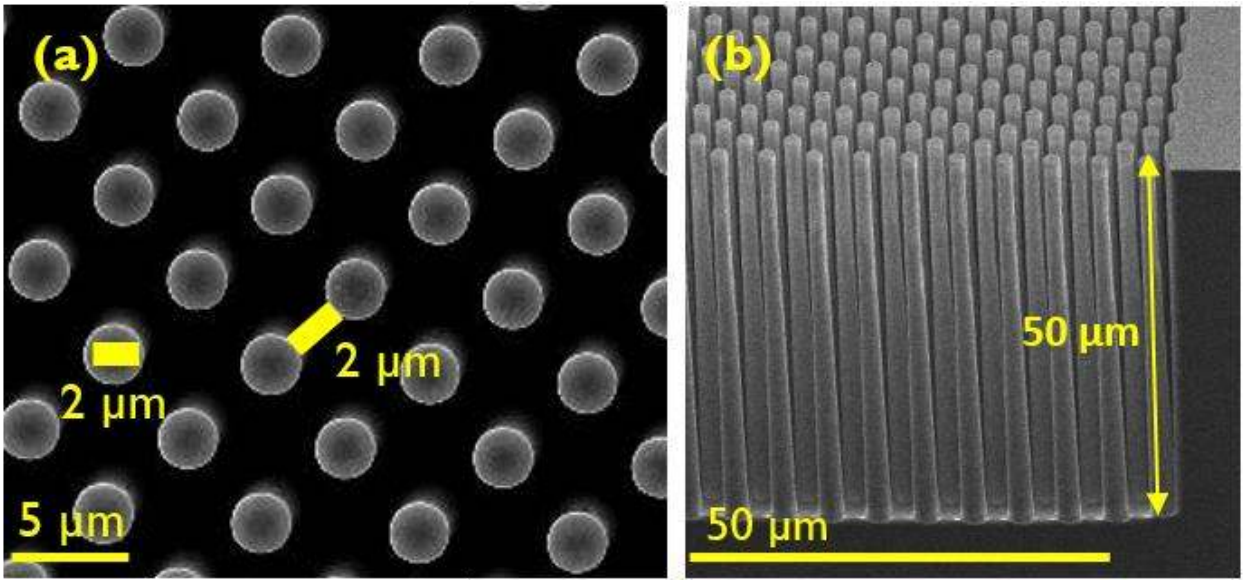

Figure S4. SEM micrographs of the TiN-coated Si micropillar array: (a) Top view of the TiN-coated Si micropillar array. (b) Tilted view of TiN-coated Si micropillar array with a Ni PVD coating.

Table S1: Atomic percentage of the elements in the Li_2CO_3 as determined by ERDA. The Li_2CO_3 was deposited by spincoating on a TiN coated substrate. After spin-coating the sample was annealed on hotplate at 110 °C for 1 min and 280 °C for 2 min.

Element	At. percentage (%)
Li	26.3
C	24.3
O	43.6
H	5.8

Table S2: Summary of the reached lithiation capacities of the LMO sample from different potential ranges ([4.4, 2.4] = full potential range, [4.4, 3.25] = 4V region and [3.25, 2.4] = 3V region) at different c-rates together with the percentage of 4V an 3V regions contributions.

C-rate	Capacity from the 4.4-2.4 V potential range ($\mu Ah/cm^2$)	Capacity from the 4.4-3.25 V potential range ($\mu Ah/cm^2$)	Capacity from the 3.25-2.4 V potential range ($\mu Ah/cm^2$)	% of the 4V region contribution*	% of the 3V region contribution*
0.1	16.52	3.5	13.02	21	79
1	15.53	5.46	10.07	35	65
2	11.79	4.06	7.73	34	66
5	11.79	4.90	6.89	42	58
10	8.26	3.50	4.76	42	58
20	8.61	4.06	4.55	47	53
50	7.14	3.22	3.92	45	55
100	4.90	1.82	3.08	37	63